PNAS RESEARCH ARTICLE | APPLIED BIOLOGICAL SCIENCES CHEMISTRY OPEN ACCESS

Modulating antigen processing through metal–organic frameworks to bias adaptive immunity

Ezra Cho[a], Meredith A. Davis[a], Julia A. Nowak[a], Mayayi Izzo[a], Anna Maria Ferrante[a], Fanrui Sha[b], Julian S. Magdalenski[b], Omar K. Farha[b], and Michelle H. Teplensky[a,c,1]

Affiliations are included on p. 12.

Edited by Catherine Murphy, University of Illinois at Urbana-Champaign, Urbana, IL; received November 7, 2024; accepted May 27, 2025

Vaccines induce specific immunity through antigen uptake and processing. However, while nanoparticle vaccines have elevated uptake, the impact of intracellular protein release and how this affects processing and downstream responses are not fully understood. Herein, we reveal how tuning unmodified antigen release rate, specifically through modulation of metal–organic framework (MOF) pore size, influences the type and extent of raised adaptive immunity. We use two MOFs in the NU-100x series with 1.4 nm difference in pore diameter, employ facile postsynthesis loading to achieve significant internalization of model protein antigen ovalbumin (*ca.* 1.4 mg/mg), and observe distinct antigen release and intracellular processing profiles influenced by MOF pore size. We investigate how this difference in release biases downstream $CD8^+$, T_H1, and T_H2 T cell responses. Ovalbumin-loaded NU-1003 induced 1.8-fold higher $CD8^+$:$CD4^+$ T cell proliferation ratio and displayed 2.2-fold greater ratio of $CD4^+$ T_H1:T_H2 cytokines compared to ovalbumin-loaded NU-1000. Antigen released from NU-1000 in vivo exhibited stronger antigen-specific IgG responses, which is dependent on $CD4^+$ T cells (up to ninefold stronger long-term antibody production and 5.9-fold higher IgG1:IgG2a ratio), compared to NU-1003. When translated to wild-type SARS-CoV-2 receptor-binding domain (RBD) protein, RBD-loaded NU-1000 induced 60.5-fold higher IgG1:IgG2a compared to NU-1003. Wild-type RBD-loaded NU-1000 immunization also induced a greater breadth of epitope recognition compared to NU-1003, as evidenced by increased binding antibodies to the Omicron RBD variant. Overall, this work highlights how antigen release significantly influences immunity induced by vaccines and offers a path to employ unmodified antigen release kinetics to drive personalized protective responses.

nanoscale vaccine design | metal–organic frameworks | adaptive immunity

Significance

Using metal–organic frameworks (MOFs) as a modulable nanoparticle vaccine platform, we investigate how intracellular protein antigen release rate biases downstream adaptive immune responses. We illustrate that while two NU-100x series MOFs load similar amounts of unmodified native protein antigen, they exhibit distinct antigen release profiles that significantly bias T cell proliferation and activity in vitro. This correlates in vivo, where mice immunized with the vaccines induce different T cell memory and varying longevity of humoral responses. Altogether, these results highlight the critical role of intracellular antigen release on eliciting a personalized immune response and these findings can be harnessed broadly to better employ native protein antigens against infectious diseases.

Vaccines can induce protective immunity against a wide range of infectious diseases including influenza, human papillomavirus, and SARS-CoV-2 (1–3). Subunit vaccines specifically raise immunity by delivering target proteins (antigens) to professional antigen-presenting cells (APCs) that result in the activation of antigen-specific adaptive immune cells (B and T cells) (4). Following delivery to an APC, the antigen must be processed to generate peptide fragments for immune propagation (5). This processing is a key parameter in modulating the resulting immunity as it profoundly impacts the downstream T cell response by determining whether antigenic peptides are presented on major histocompatibility complex (MHC)-I (for $CD8^+$ T cell activation) or MHC-II (for $CD4^+$ T cell activation) (6). Furthermore, antigen release rate can influence the subset of $CD4^+$ T cell activation (i.e., T_H1 versus T_H2) (6).

Proteins are naturally unstable, and thus once internalized through endolysosomal pathways for normal processing, they are subject to rapidly being acted on by processing enzymes. Moreover, prior to delivery to an APC, free native proteins are highly susceptible to degradation within the body (7). As such, recent strategies have incorporated nanotechnology, such as polymeric and lipid-based nanoparticles, to more effectively deliver immunogenic cargo to APCs (8–10). Once inside, these nanocarriers must release their protein antigen cargo to be processed into the necessary peptide fragments. However, current nanoparticle delivery approaches are limited in their ability to affect this antigen release and processing rate due to nanoparticle instability, incompatible solvent conditions for loading proteins without employing genetic modifications to the protein, and the inability to maintain stabilization of protein antigens in cell-imposed stresses (11–14). While recognized as an important parameter in modulating vaccine efficacy, (15) antigen release kinetics using nanoparticle systems has mainly focused on affecting the release of antigenic peptides due to the limitations of current technology (16–18). Moreover, the ability to achieve tuned antigen release using native, unmodified protein antigen has also been unrealized. An

Author contributions: E.C. and M.H.T. designed research; E.C., M.A.D., J.A.N., M.I., A.M.F., F.S., J.S.M., and M.H.T. performed research; E.C., F.S., J.S.M. and M.H.T. analyzed data; and E.C., M.A.D., J.A.N., M.I., A.M.F., F.S., J.S.M., O.K.F., and M.H.T. wrote the paper.

Competing interest statement: O.K.F. has a financial interest in Numat, a startup company that is seeking the commercialization of MOFs.

This article is a PNAS Direct Submission.

M.H.T. is an organizer of this Special Feature.

[1]To whom correspondence may be addressed. Email: mtep@bu.edu.

This article contains supporting information online at https://www.pnas.org/lookup/suppl/doi:10.1073/pnas.2409555122/-/DCSupplemental.

Published November 3, 2025.

alternative approach to tune this rate genetically modifies a protein antigen's amino acid sequence. Disadvantageously, this method is inherently protein-specific, requires research for each newly identified antigen, and can lead to critical modifications of immunogenic amino acids and loss of function (19–21).

Herein, we harness metal–organic framework (MOF) nanoparticles to address this gap. MOFs are highly porous crystalline nanomaterials composed of metal nodes coordinated to organic linkers (22, 23). Due to their tunable synthesis, MOFs can be synthesized with a range of metal nodes and organic linkers (24). These can be designed to be highly biocompatible and with large pore sizes ideal for cargo encapsulation through electrostatic entrapment (25–28). MOFs have been extensively utilized for gas storage and catalysis, among other fields, due to these selective interactions (29–34). However, recent work has explored their implementation in biomedical applications, such as drug delivery (27, 28, 35–39). In particular, the NU-100x series (where x = 0 to 7) is a range of zirconium-based MOFs that can be modularly synthesized with different linkers to generate pores ranging from 3.3 to 6.7 nm in diameter (24). Prior work has confirmed the biocompatibility of these materials (28, 40). The high degree of modularity within the NU-100x MOF series allows us to evaluate how modifying the pore size, while maintaining the channel-type csq topology, alters the antigen release profile. We hypothesize that changes to the pore size will alter the electrostatic interactions with protein during loading within the MOFs, and that this will alter the antigen release rate, antigen processing pathway, and thus bias: 1) $CD8^+$ and $CD4^+$ T cell activation and 2) T_H1 and T_H2 cell polarization.

In this work, we employ two nano-sized MOFs in this series of varying pore sizes, NU-1000 (3.3 nm pore) and NU-1003 (4.7 nm pore), to alter the antigen release rate and affect intracellular processing. We observed that both NU-1000 and NU-1003 nanoparticles are capable of loading significant quantities of native, unmodified protein antigen, outcompeting some traditional vaccine delivery systems (41, 42). We measured how changes to the release kinetics altered APC processing and enhanced MHC-I antigen presentation in bone marrow–derived dendritic cells (BMDCs). This processing resulted in differences in downstream propagation of antigen-specific T cell responses. Ovalbumin antigen-loaded NU-1000 (Ova@NU-1000) induced greater $CD4^+$ responses compared to equivalent doses of ovalbumin antigen-loaded NU-1003 (Ova@NU-1003), while Ova@NU-1003 biased a $CD8^+$ and T_H1 subtype in vitro. When the MOFs were each coadministered with adjuvant in addition to antigen to build an effective vaccine, we observed that the NU-1000 vaccine induced strong antigen-specific $CD8^+$ and $CD4^+$ T cells as well as stronger $CD4^+$ T cell–based humoral responses long-term. Meanwhile, NU-1003 favored total $CD8^+$ T cell and T_H1 responses in vivo. When applying our system to clinically relevant wild-type SARS-CoV-2 receptor-binding domain (RBD) protein, we corroborated our results and observed that antigen-loaded NU-1000 (RBD@NU-1000) induced a greater breadth of epitope recognition in its humoral response. Antigen-loaded NU-1003 (RBD@NU-1003) maintained its preference toward inducing a T_H1 response. Ultimately, these results uncover how the adaptive immune response can be biased by harnessing vaccine release kinetics, which can be facilely controlled through the modular architecture in NU-100x series MOFs.

Results

Postsynthetic MOF Loading with Protein Antigen. We selected NU-1000 and NU-1003 to investigate the effects of antigen release kinetics on downstream adaptive immune responses. These MOFs were selected because their sole difference is a 1.4 nm pore increase, and both MOFs are capable of being synthesized at biologically relevant nanoscale sizes (100 to 200 nm) (*SI Appendix,* Fig. S1 *A* and *B*). These nanoparticle sizes were employed to be biologically advantageous for entry into immune cells to deliver encapsulated antigen, as well as future in vivo considerations (43). Their large pore sizes following synthesis were validated against micrometer-sized versions of the same MOFs (24) using nitrogen isotherms (*SI Appendix,* Fig. S2). A key advantage of NU-100x series MOFs is their capacity to encapsulate native proteins, stemming from their large pore sizes. These pores can also successfully protect proteins from harsh environments and entrap them to prevent leaching, while still ultimately enabling normal protein function (25). Thus, we harnessed a facile postsynthetic loading method to load large quantities of protein antigen into NU-1000 and NU-1003 MOFs.

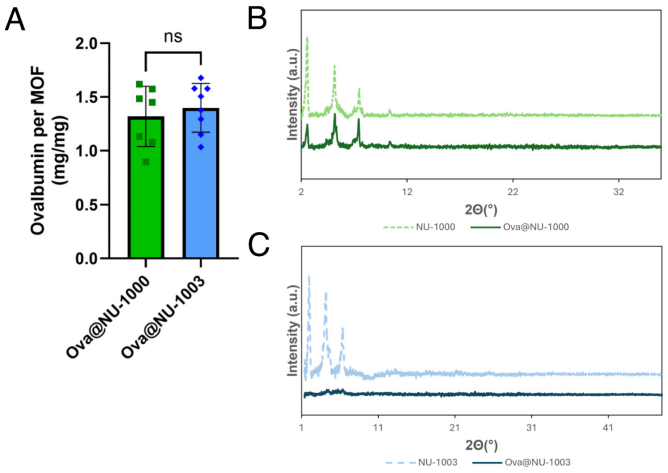

Fig. 1. NU-1000 and NU-1003 successfully load high quantities of native ovalbumin protein antigen. (*A*) NU-1000 and NU-1003 load similar quantities of ovalbumin (n = 7 to 8 per group). Mean and SD shown. (*B* and *C*) Background-subtracted PXRD of NU-1000 (*B*) or NU-1003 (*C*) unloaded (dashed lines) and loaded (solid lines) MOFs illustrates the drop in crystallinity following antigen loading. In panel *A*, analysis was performed using an unpaired, two-tailed *t* test. ns = non-significant.

We selected the model protein antigen ovalbumin (Ova) to investigate the kinetics and immune responses with commercially available tools. NU-1000 and NU-1003 were loaded through incubation in an aqueous solution of ovalbumin (100 μM). Encapsulation was determined using a bicinchoninic acid assay (BCA) by quantifying the ovalbumin remaining in the supernatant relative to the initial encapsulation concentration. These encapsulated MOFs, termed Ova@NU-1000 and Ova@NU-1003, were determined to load *ca.* 1.4 mg/mg of ovalbumin to MOF (Fig. 1*A*). No significant difference in total loading quantity was observed with these two nanoparticles. Ovalbumin loading into the pores of the MOFs was further validated using powder X-ray diffraction (PXRD) (Fig. 1 *B* and *C* and *SI Appendix,* Fig. S3 *A* and *B*), which has been previously used as a proxy for pore occupation of biomolecular cargo (27, 44). The PXRD highlights that ovalbumin occupies a majority of the MOF pore space, as observed by the pronounced drop in MOF crystallinity based on observed peaks in loaded MOFs compared to unloaded MOFs. Though both MOFs loaded similar amounts of ovalbumin, we observed a greater drop in PXRD signal contrast for Ova@NU-1003. We attribute this greater decrease to the more fragile crystallinity of the NU-1003 structure as a result of the larger pore size. Ova@MOFs were also analyzed via scanning electron microscopy (SEM), which showed no significant differences in size following ovalbumin encapsulation (*SI Appendix,* Fig. S4).

Antigen Release Kinetics and Processing of Ova@NU-100x MOFs. To achieve effective intracellular antigen delivery and assess the varied processing kinetics between the pore sizes, we evaluated how Ova@MOFs release antigen in endolysosomal conditions. We loaded NU-1000 and NU-1003 with fluorophore-conjugated ovalbumin (Ova-AF555@MOFs) for easy tracking of the antigen, and incubated the complexes in acidic (pH 6.5) phosphate-buffered saline (PBS) supplemented with 10% fetal bovine serum (FBS) to investigate the release of ovalbumin over time and mimic physiological conditions in the endolysosome. Ova-AF555@NU-1000 showed a burst release of *ca.* 27% of its total antigen in the first half hour and *ca.* 41% release within the first 2 h, after which it steadily released the remaining cargo over 7 d (Fig. 2 *A* and *B*). Meanwhile, Ova-AF555@NU-1003 exhibited a slower release profile with a burst release of *ca.* 5% in the first half hour that reached *ca.* 40% by 48 h (Fig. 2 *A* and *B*). Both MOFs released equivalent total antigen by 7 d. We calculated from the release curves that NU-1000 exhibited a faster release rate during the initial 6 h, but NU-1003 overtook it and exhibited a faster release rate for the remaining 7 d (*SI Appendix*, Fig. S5). We attribute this difference to the larger pores of NU-1003, and thus expect weaker electrostatic interactions compared to NU-1000, which we hypothesize could allow proteins to penetrate deeper into the MOF nanoparticle during the protein-MOF loading process and thus delay their subsequent release from the MOF.

To evaluate the processing of the nanoparticles with these differing release profiles, we first investigated the timescale of Ova@MOF uptake into APCs in vitro. Murine BMDCs were incubated with Ova@MOFs for up to 24 h. Samples were analyzed via flow cytometry by using the MOF's inherent fluorescent signal (emission ~387 nm (28)) to track particle uptake. Both Ova@NU-1000 and Ova@NU-1003 exhibited similar BMDC uptake profiles. Ova@MOFs were continuously taken up until 6 h, although the fastest rate of uptake occurred during the first hour (Fig. 2*C*). Furthermore, both Ova@MOFs showed a decreased signal after 6 h, likely due to intracellular degradation and processing. This degradation is further supported by the median fluorescence intensity (MFI) distributions, which begin as a growing unimodal

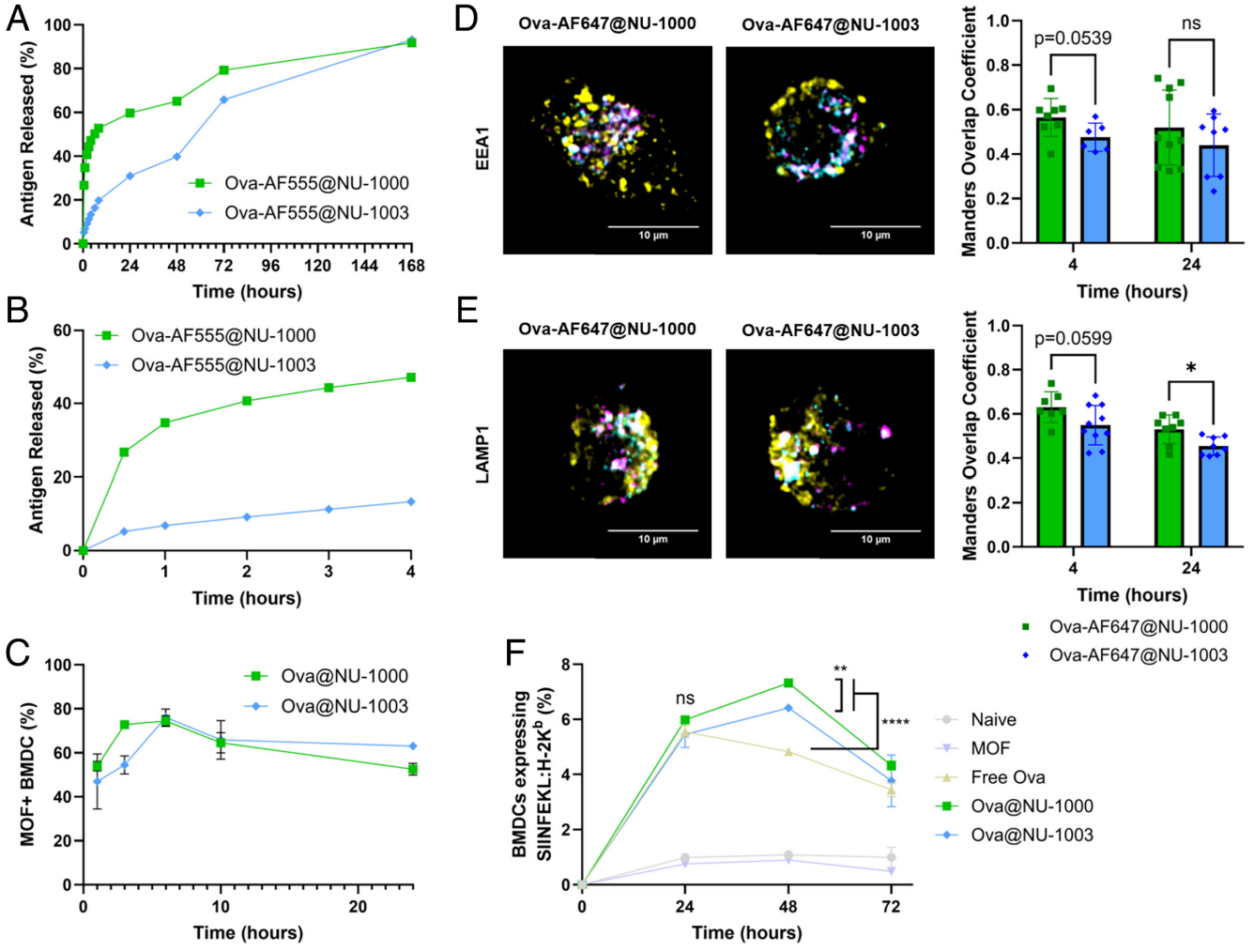

Fig. 2. MOF pore size changes the antigen profile and cell uptake, which influences downstream processing kinetics. (*A*) Ovalbumin is released more rapidly from Ova-AF555@NU-1000 compared to Ova-AF555@NU-1003. (*B*) Inset of the first 4 h of release in (*A*). (*C*) Ova@MOF is taken up by BMDCs to similar extents over 24 h. Differences in the timecourse of the uptake are shown between the two different nanoparticles (n = 3 per group). (*D* and *E*) Representative cell images and colocalization of Ova-AF647 (magenta) and early endosome measured through EEA1 (*D*) or lysosome measured through LAMP1 (*E*) (yellow) from isolated BMDCs treated with Ova-AF647@NU-1000 and Ova-AF647@NU-1003 for 4 or 24 h (n = 6 to 10 per group). MOF is cyan. Mander's overlap coefficient representing the fraction of Ova-AF647 signal colocalized with the respective organelle are shown. (*F*) Ova@MOF delivery to BMDCs enhances antigen presentation of MHC-I-restricted SIINFEKL epitope over 72 h compared to Free Ova (n = 2 per group). All groups were treated with 2.5 μM of ovalbumin antigen and 2.5 μM of ODN1826 adjuvant. Signal intensity is most elevated after 48 h for Ova@NU-1000 compared to Ova@NU-1003. Mean and SD shown in panels *C*–*F*. In panels *D* and *E*, analysis was performed using an unpaired, two-tailed *t* test within each timepoint. In panel *F*, analysis was performed using an ordinary two-way ANOVA, followed by a Tukey's multiple comparisons test. *P = <0.05; **P < 0.01; ****P < 0.0001; ns = non-significant. Not all comparisons shown for simplicity.

population as BMDCs take up Ova@MOF, but become bimodal with one peak closer in intensity to the untreated condition as the MOF within the cells degrades over time (*SI Appendix*, Fig. S6).

We then investigated differences in intracellular antigen processing. NU-1000 and NU-1003 were loaded with fluorophore-conjugated ovalbumin (Ova-AF647@MOFs) and incubated with BMDCs for 4 or 24 h. Cells were stained to observe antigen colocalization with early endosomes via the Early Endosome Antigen 1 (EEA1) marker or with lysosomes via the Lysosome Associated Membrane Glycoprotein 1 (LAMP1) marker. At both timepoints, ovalbumin encapsulated within NU-1000 exhibited greater colocalization with both intracellular compartments compared to ovalbumin in NU-1003, though the difference is more prominent with lysosomal colocalization (Fig. 2 *D* and *E*). Given its faster release rate, this supports that NU-1000 skews toward greater MHC-II-based processing, as for this process, antigen is loaded onto MHC-II in the lysosome (45). Conversely, the reduced colocalization between ovalbumin and both intracellular compartments mediated through NU-1003 suggests that greater antigen release is occurring outside endolysosomal compartments, which facilitates MHC-I-based cross-presentation (46).

To explore the downstream impact of MOF pore size altering ovalbumin processing, we evaluated antigen presentation and specifically the upregulation of the identified SIINFEKL epitope on MHC-I (SIINFEKL:H-2K^b) using a commercially available antibody. We incubated BMDCs with ovalbumin as either free protein or within Ova@MOFs in a mixture containing ODN1826 toll-like receptor (TLR) 9 adjuvant to stimulate antigen presentation for 24, 48, and 72 h. Ovalbumin administration regardless of the vaccine formulation or vehicle elevated the presentation of SIINFEKL on H-2K^b to *ca.* 5.5-6% of BMDCs by 24 h (Fig. 2*F*). However, the signal intensity decreased to *ca.* 4.8% after 48 h for free ovalbumin treatment, whereas for Ova@MOF treatments, the SIINFEKL:H-2K^b signal increased to *ca.* 7.3% and 6.4% for Ova@NU-1000 and Ova@NU-1003, respectively (Fig. 2*F* and *SI Appendix*, Fig. S7). This elevated signal was absent for naïve BMDCs or those treated with unloaded MOF, verifying that the signal is directly due to effective antigen delivery through ovalbumin encapsulation within the MOFs (Fig. 2*F* and *SI Appendix*, Fig. S7).

This elevated antigen presentation compared to the free Ova treatment can be attributed to the elongated kinetics of MOF cargo release. Furthermore, this increase for Ova@MOF nanoparticle treatment, in contrast to the decrease with free ovalbumin treatment, highlights that the MOF effectively protects antigen until it is ultimately processed intracellularly. The statistically significant difference for SIINFEKL:H-2K^b presentation between Ova@NU-1000 and Ova@NU-1003 (*ca.* 1% more BMDCs presenting SIINFEKL) can be attributed to the overall increased antigen release within the time period exhibited by Ova@NU-1000 (Fig. 2*A*). As the presentation of SIINFEKL requires cross-presentation, these data illustrate that both Ova@MOFs entrap and deliver significant antigen, and both are capable of releasing antigen into the cytosol for cross-presentation. Ova@MOF delivery increased CD80 costimulatory marker expression, likely attributed to the MOF encapsulating and delivering the coadministered ODN1826 (*SI Appendix,* Fig. S8). As both Ova@NU-100x treatments induced similar innate activation, this emphasizes the role of the differing antigen release kinetics and spatial processing on affecting antigen presentation and downstream T cell activation. Moreover, these data validate that internalization of the native protein antigen within a MOF does not negatively affect the ability of the antigen to be processed into immunogenic epitopes. We proceeded to next investigate how differences in antigen processing modulate downstream T cell propagation in response to presentation of this epitope and the MHC-II-restricted "Ova2" epitope.

Antigen Release Rate from MOFs Biases T Cell Activity and Subtypes In Vitro. Having established differing antigen release kinetics between the two Ova@MOFs and having observed successful SIINFEKL presentation on MHC-I by BMDCs, we explored how differences in antigen processing bias the activation of antigen-specific CD4$^+$ and CD8$^+$ T cells. We incubated Ova@MOFs with either stained OT-I or OT-II splenocytes, isolated from transgenic mice with either CD8$^+$ or CD4$^+$ T cells expressing T cell receptors specific to the Ova1 (SIINFEKL) or Ova2 (ISQAVHAAHAEINEAGR) sequence of ovalbumin, respectively. As these cells exhibit strong ovalbumin-specific responses, they were used to investigate the strength of CD8$^+$ and CD4$^+$ T cell proliferation driven from the different antigen release rates of the Ova@MOFs. After 3 d of treatment with various doses, cells were analyzed via flow cytometry. We quantified an EC_{50} of 161.8 nM and 36.19 nM for OT-I and OT-II proliferation, respectively, for Ova@NU-1000 (*SI Appendix,* Fig. S9 *A* and *B*). This EC_{50} was *ca.* 1.8-fold and 13.9-fold more potent than free ovalbumin for CD8$^+$ and CD4$^+$ T cell proliferation (EC_{50} = 296.9 nM and 503.6 nM, respectively; *SI Appendix,* Fig. S9 *A* and *B*). Interestingly, Ova@NU-1003 exhibited a *ca.* 1.8-fold more potent EC_{50} (89.59 nM) for OT-I proliferation compared to its NU-1000 counterpart, however a significantly weaker EC_{50} for OT-II proliferation (610.6 nM; *SI Appendix*, Fig. S9 *A* and *B).* These defined differences in CD8$^+$ and CD4$^+$ T cell proliferation illustrate the bias mediated by different antigen release rates through MOF pore size.

To recapitulate a more comprehensive immune response, as well as determine a preferential activation of CD8$^+$ or CD4$^+$ antigen-specific responses, Ova@MOFs were cultured with pooled splenocytes from both OT-I and OT-II mice and analyzed after 3, 4, or 5 d (Fig. 3*A* and *SI Appendix,* Fig. S10). On day 4, we quantified that Ova@NU-1000 elicited both significant antigen-specific CD8$^+$ and CD4$^+$ T cell proliferation (EC_{50}: 1.99 and 55.34 nM, respectively) (Fig. 3 *B* and *C*). These values are significantly lower than free ovalbumin (562.4 and 2479 nM for OT-I and OT-II proliferation, respectively; Fig. 3 *B* and *C*). Notably, Ova@NU-1003 exhibited a much less potent EC_{50} of 3916 nM for OT-II proliferation (Fig. 3*C*). While the EC_{50} for OT-I proliferation was still weaker than that of Ova@NU-1000 (44.88 nM for Ova@NU-1003), overall this shows a clear bias toward CD8$^+$ proliferation for the Ova@NU-1003 delivery. These trends were consistent across multiple timepoints (3 and 5 d), where Ova@NU-1000 induced the strongest OT-I and OT-II proliferation, and Ova@NU-1003 induced strong OT-I and much weaker OT-II proliferation (*SI Appendix,* Fig. S11).

When investigating a single treatment at 10 nM, we quantified that Ova@NU-1000 induced between a *ca.* 6.8 to 10.9-fold higher increase in CD8$^+$ and *ca.* 2.5 to 6.2-fold increase in CD4$^+$ T cell proliferation compared to free ovalbumin (Fig. 3 *D* and *E*). Meanwhile, Ova@NU-1003 induced between a *ca.* 2.9 to 7.7-fold increase in CD8$^+$ and *ca.* 0.8 to 3.0-fold increase in CD4$^+$ T cell proliferation compared to free ovalbumin (Fig. 3 *D* and *E*). This leads to Ova@NU-1000 inducing a CD8$^+$:CD4$^+$ T cell proliferation ratio of *ca.* 2 while Ova@NU-1003 induced a ratio of *ca.* 3 across all days (Fig. 3 *D* and *E*). These results highlight the significant opportunity to design personalized vaccines against diseases that require stronger CD8$^+$ or CD4$^+$ responses that can be mediated solely via native antigen release. As exhibited herein, the antigen required no modifications to the amino acid sequence to bias these profiles, which can be useful when specific immunogenic epitopes are unknown.

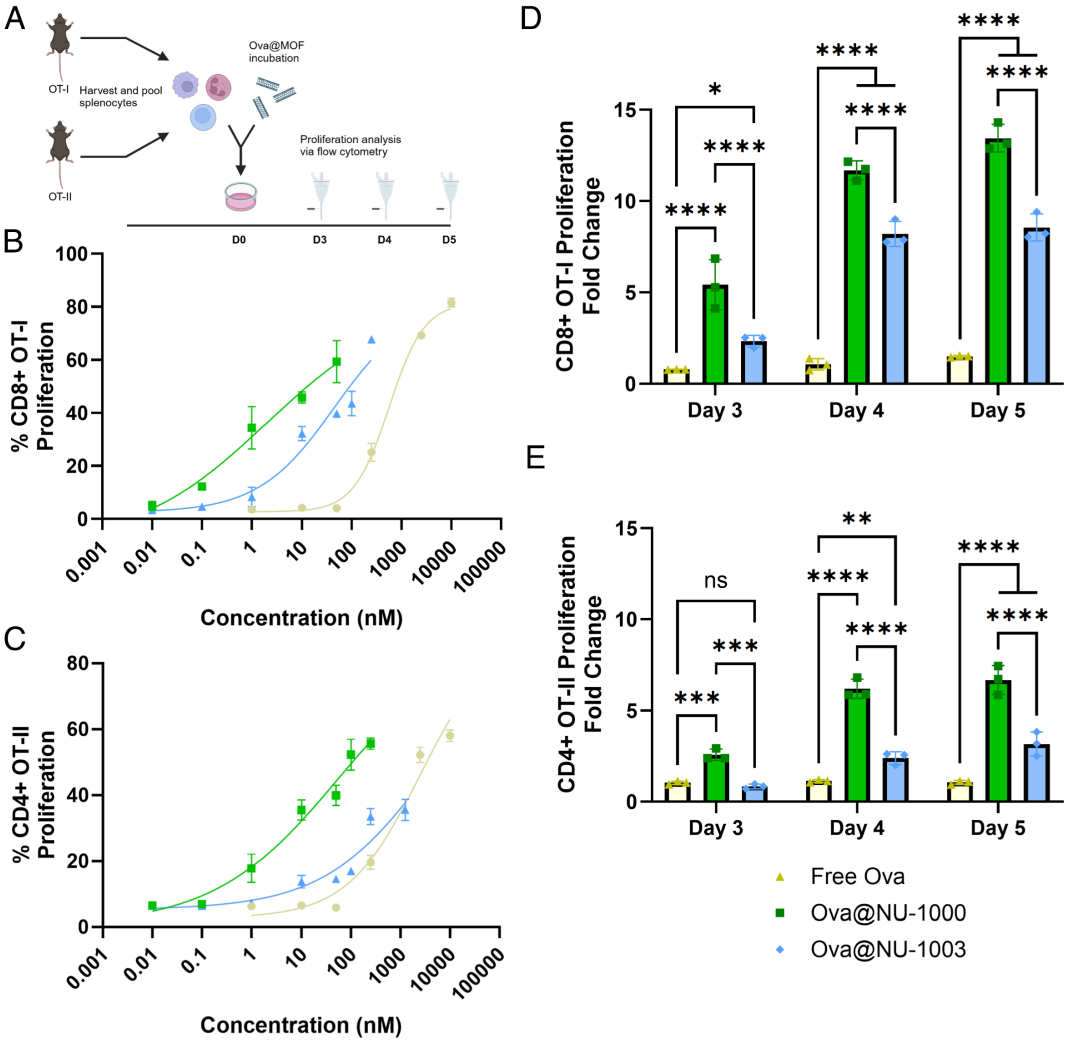

Fig. 3. Ova@NU-1000 and Ova@NU-1003 elicit distinct T cell proliferation profiles in vitro. (*A*) Splenocytes from OT-I and OT-II mice were harvested, stained, and pooled before incubating with free ovalbumin or antigen loaded within NU-100x (Ova@NU-100x). Cells were collected 3 to 5 d following incubation and stained for live flow cytometric analysis. Created with BioRender.com. (*B* and *C*) Proliferation dose–response curves of $CD8^+$ OT-I (*B*) and $CD4^+$ OT-II (*C*) T cells after 4 d of incubation (n = 3 per group). (*D* and *E*) Proliferation fold change of $CD8^+$ OT-I (*D*) and $CD4^+$ OT-II (*E*) T cells treated at 10 nM by Ova following 3 to 5 d of incubation, compared to untreated cells (n = 3 per group). Mean and SD shown in *B*–*E*. In panels *D* and *E*, analysis used an ordinary two-way ANOVA, followed by a Tukey's multiple comparisons test. *$P < 0.05$; **$P < 0.01$; ***$P < 0.001$; ****$P < 0.0001$; ns = nonsignificant.

We also measured T cell activity through the production of interferon gamma (IFN-γ), which was quantified via ELISA on supernatant from pooled OT-I and OT-II splenocytes 4 d following incubation with the Ova@MOFs at 1000 nM treatment concentration. Both Ova@NU-1000 and Ova@NU-1003 induced significantly higher levels of IFN-γ secretion compared to free ovalbumin (Fig. 4*A*). Indeed, we measured a *ca.* 10.9-fold increase by Ova@NU-1000 and *ca.* 8.8-fold increase by Ova@NU-1003 compared to free ovalbumin. The significantly higher IFN-γ production induced by Ova@NU-1000 can be attributed to the aforementioned stronger $CD4^+$ and $CD8^+$ T cell antigen-specific proliferation in the pooled coculture.

While IFN-γ has been used to illustrate overall immune activity (47), $CD4^+$ T cells produce varying cytokines to direct the immune response depending on the pathological threat (48). Notably, T_H1 cells promote cellular immunity through IFN-γ secretion while T_H2 cells promote humoral immunity through interleukin (IL)-5 secretion, though overlap can exist between the phenotypes (48). As $CD4^+$ T cells are the primary producers of IL-5, we first investigated its production in OT-II splenocytes. When treated with 250 nM of Ova@MOF, Ova@NU-1000 induced a *ca.* 16.4-fold increase in IL-5 secretion compared to Ova@NU-1003, despite producing comparable levels of IFN-γ (*SI Appendix*, Fig. S12 *A* and *B*). The ratio of IFN-γ:IL-5 cytokines in these cells provides insights for a MOF-mediated bias toward a T_H1 versus T_H2 phenotype. Ova@NU-1000 induced an IFN-γ:IL-5 ratio of *ca.* 700, *ca.* 14-fold lower than that induced by Ova@NU-1003 (*SI Appendix*, Fig. S12*C*). These results suggest that Ova@NU-1003 skews toward a T_H1 $CD4^+$ T cell phenotype, which influences the long-term cellular and humoral responses (49). These findings were consistent when evaluating cytokines secreted from pooled OT-I and OT-II splenocytes. At 1000 nM, both Ova@MOFs secreted more IL-5 compared to free ovalbumin and controls of naïve splenocytes and unloaded MOF. However, Ova@NU-1000 produced *ca.* 2.7-fold greater IL-5 cytokine compared to Ova@NU-1003 (Fig. 4*B*), resulting in a *ca.* 2.2-fold lower ratio of IFN-γ:IL-5 (ratios of *ca.* 1385 and 3111, respectively) (Fig. 4*C*). These results highlight how the slower antigen release rate kinetics mediated through NU-1003 bias raised immunity toward $CD8^+$ and T_H1 T cell responses.

MOF Architecture Biases the Raised Adaptive T Cell Response and Memory Generated In Vivo. Given the observed differences in T cell proliferation, we evaluated how the Ova@MOFs distinctly propagate adaptive immune memory in vivo. As the loaded MOFs

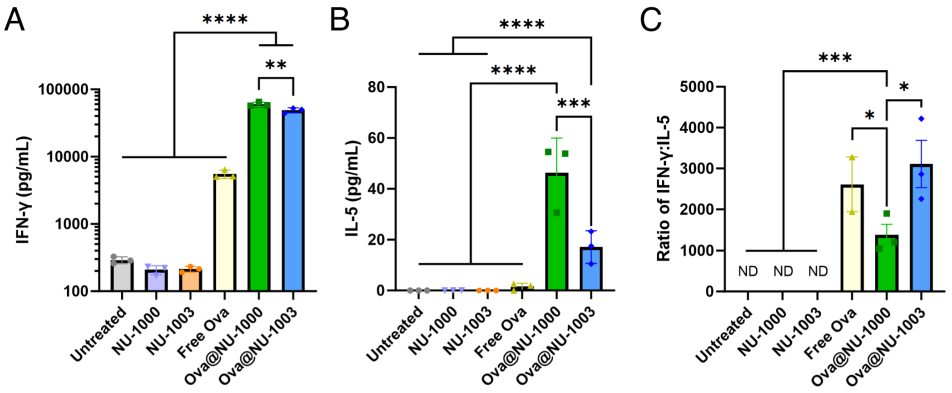

Fig. 4. Ova@NU-1000 and Ova@NU-1003 elicit distinct T_H1 and T_H2 cytokine profiles. (*A* and *B*) Ova@MOFs induce greater quantities of IFN-γ (*A*) and IL-5 (*B*) compared to free ovalbumin in pooled OT-I and OT-II splenocytes following 4 d of incubation with 1000 nM of treatments by Ova (n = 3 per group). (*C*) Ova@NU-1000 and Ova@NU-1003 induce distinct ratios of IFN-γ:IL-5 cytokines in pooled OT-I and OT-II splenocytes following 4 d of incubation (n = 3 per group). Mean and SEM shown in all graphs. Analysis used an ordinary one-way ANOVA, followed by Tukey's (*A* and *C*) or Šídák's (*B*) multiple comparisons test. $^*P < 0.05$; $^{**}P < 0.01$; $^{***}P < 0.001$; $^{****}P < 0.0001$. ND = not detected. Not all significances shown for clarity.

thus far solely employed antigen protein, we added adjuvant to the nanostructure by coencapsulating TLR9 agonist ODN1826 to elevate immunostimulatory capabilities (termed Adj-Ova@NU-1000 and Adj-Ova@NU-1003). NU-1000 and NU-1003 were loaded with a *ca.* 1:1 molar ratio of ODN1826 to ovalbumin in both MOFs (*SI Appendix,* Fig. S13).

Female C57BL/6 mice (n = 3-4) were injected with either an admix of free adjuvant and ovalbumin protein or a coencapsulation of adjuvant and ovalbumin within a MOF. Animals were boosted twice every other week, and then euthanized on day 35 to analyze their cellular immune response raised in splenocytes (Fig. 5*A*). Adaptive cellular memory was first investigated by measuring $CD44^+CD62L^-$ effector memory T cells (T_{EM}). All vaccination conditions trended toward an elevated $CD4^+$ T_{EM} population, but statistical significance was not observed (Fig. 5*B* and *SI Appendix,* Fig. S14). We attribute the lack of significant changes from Adj-Ova@NU-1000 or Adj-Ova@NU-1003 in modulating $CD4^+$ T_{EM} responses to the sensitivity of the assay and low dose utilized (employing solely 2 nmol each of antigen and adjuvant). However, Adj-Ova@MOF treatments elevated $CD8^+$ T_{EM} cells, with Adj-Ova@NU-1003 inducing a *ca.* 7.8% higher population of T_{EM} cells compared to the admix (Fig. 5*C* and *SI Appendix,* Fig. S14). These results coincide with the in vitro findings and corroborate that Adj-Ova@NU-1003 primarily biases a strong $CD8^+$ T cell response.

We further examined whether the T cell population raised was specific by quantifying Ova1-specific $CD8^+$ and Ova2-specific $CD4^+$ T cells. We measured a *ca.* 2.1-fold and *ca.* 1.7-fold increase in Ova1-specific $CD8^+$ T cells, and a *ca.* 1.7-fold and *ca.* 1.4-fold increase in Ova2-specific $CD4^+$ T cells from Adj-Ova@NU-1000 and Adj-Ova@NU-1003, respectively, compared to admix (Fig. 5 *D* and *E* and *SI Appendix,* Figs. S15 and S16). Given that these represent a portion of the total splenic $CD8^+$ or $CD4^+$ T cells and that this assay only investigates a single possible MHC-I- and MHC-II-restricted epitope within the protein antigen, these results illustrate that both Adj-Ova@MOFs can establish robust antigen-specific $CD8^+$ T cell responses, while Adj-Ova@NU-1000 establishes robust antigen-specific $CD4^+$ T cells.

To further investigate the ability of raised $CD8^+$ T cells to respond to antigen-specific stimuli, we performed an IFN-γ ELISpot by restimulating splenocytes ex vivo with Ova1 peptide. There were *ca.* 85 and 91 spot-forming cells (SFCs) from Adj-Ova@NU-1000 and Adj-Ova@NU-1003 immunization, respectively (Fig. 5*F*). No counts were observed for unstimulated splenocytes, nor those stimulated with a nonspecific antigen, highlighting the strong and specific response elicited by both Adj-Ova@MOFs. These findings also illustrate that both Adj-Ova@NU-1000 and Adj-Ova@NU-1003 vaccines maintain protein cargo stability in vivo until the antigen is released in APCs for processing and subsequent MHC presentation. Overall, these findings indicate Adj-Ova@NU-1000 induces both robust $CD4^+$ and $CD8^+$ T cell responses while Adj-Ova@NU-1003 strongly biases a $CD8^+$ T cell response due to antigen release kinetics and processing.

MOF Architecture Induces Distinct Long-Term Adaptive Humoral Immune Responses In Vivo. We next investigated the humoral response mediated by $CD4^+$ T cells to understand the nuances in MOF-induced $CD4^+$ T cell subtypes (48). We first sought to validate the specificity of antibody production and determine the dose threshold for ovalbumin-specific antibody production through MOF-mediated delivery and release. For this, we analyzed the build-up of ovalbumin-specific IgG antibodies following multiple Ova@MOF injections. We focused on NU-1000 to evaluate the dose dependence, as we expected a similar dose dependence from NU-1003 nanoparticles. Female C57BL/6 mice (n = 3) were treated on day 0 and 7 with either a dose of 0.25 or 1 nmol of both ovalbumin antigen and ODN1826 adjuvant, followed by a blood draw on day 21. The 1 nmol dose of Ova@NU-1000 induced significant ovalbumin-specific IgG antibody responses (ovalbumin-specific IgG reciprocal endpoint titer of *ca.* 1300) that are *ca.* 4.4-fold greater than the equivalently dosed admix vaccine (Fig. 6*A*). Critically, a 0.25 nmol Ova@NU-1000 dose significantly induced antibodies (reciprocal endpoint titer of *ca.* 100), which was not statistically different to that of admix immunization given at a fourfold higher dose (Fig. 6*A*). Importantly, the unloaded NU-1000 nanoparticle alone did not raise ovalbumin-specific antibodies, highlighting that the MOF itself does not induce immunity but instead facilitates the immunogenicity of its cargo (Fig. 6*A*). The significant responses from ovalbumin-loaded NU-1000 treatment illustrates that the antibody response can be used as a surrogate to interrogate how antigen release rate impacts $CD4^+$ T cell–mediated downstream activity. To understand how antigen release from NU-1000 and NU-1003 nuances the $CD4^+$ T cell response, we immunized female C57BL/6 mice (n = 3) with 2 nmol of both ovalbumin antigen and ODN1826 adjuvant coencapsulated in an admix, Adj-Ova@NU-1000, or Adj-Ova@NU-1003 on day 0, then boosted twice every other week (weeks 2 and 4). Blood was drawn on weeks 3 to 5 to investigate the humoral response. Throughout the study, both Adj-Ova@NU-1000 and Adj-Ova@NU-1003 vaccines induced stronger ovalbumin-specific antibody responses compared to the

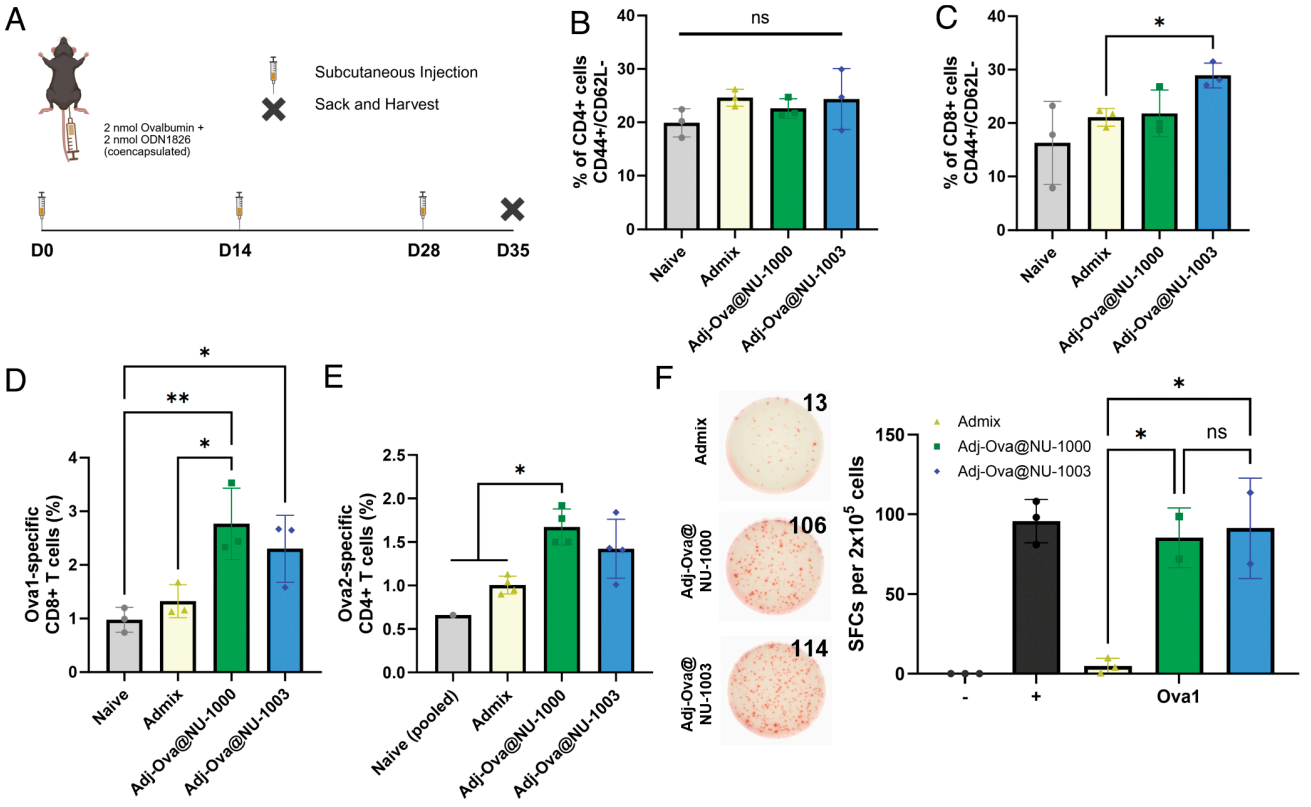

Fig. 5. Adj-Ova@NU-1000 and Adj-Ova@NU-1003 elicit strong ovalbumin-specific $CD8^+$ T cell responses in vivo. (*A*) Female C57BL/6 mice (n = 3-4 per group) were treated with 3 immunizations of ovalbumin and ODN1826 as an admix or in Adj-Ova@MOFs and euthanized as per the schedule shown. Created with BioRender.com. (*B* and *C*) Comparisons of $CD44^+CD62L^-$ effector memory $CD4^+$ (*B*) and $CD8^+$ (*C*) T cells between the different treatments (n = 3 per group). (*D* and *E*) Comparisons of $CD8^+$ T cells specific to the MHC-I-restricted Ova1 epitope (*D*) and $CD4^+$ T cells specific to the MHC-II-restricted Ova2 epitope (*E*) of ovalbumin (n = 3-4 per group). (*F*) Comparisons of IFN-γ-producing T cells following ex vivo restimulation with the Ova1 peptide (n = 2-3 per group). (*Left*) Representative images showing raw counts and (*Right*) quantified spot forming cells (SFCs) per 2×10^5 splenocytes. Mean and SD shown in panels *B*–*F*. In panels *B* and *C*, analysis was performed using Brown-Forsyth and Welch's ANOVA followed by Dunnett's T3 multiple comparisons test. In panels *D*–*F*, an ordinary one-way ANOVA, followed by Tukey's multiple comparisons test. $*P < 0.05$; $**P < 0.01$; ns = nonsignificant. Not all significances are shown for clarity.

admix (Fig. 6*B*). All antibody responses peaked at 5 wk (*ca.* 450, 11000, and 18000 for admix, Adj-Ova@NU-1000, and Adj-Ova@NU-1003, respectively). No significant difference was observed in antibody titers between Adj-Ova@NU-1000 and Adj-Ova@NU-1003. As a result of this finding, we hypothesized that significant differences in $CD4^+$ T cell biasing observed through NU-1000-mediated antigen release require an extended kinetic evaluation to effectively detect as well as a decreased dose to better resolve differences between the structures.

To investigate long-term biases in affected humoral responses, female C57BL/6 mice (n = 2-3) were injected with 1 nmol of ovalbumin antigen as either Ova@NU-1000 or Ova@NU-1003 with equivalent 1 nmol ODN1826 adjuvant on weeks 0 and 1, followed by blood draws on weeks 3, 4, 5, and 7 (*SI Appendix*, Fig. S17). Both treatments showed similar ovalbumin-specific IgG antibody titer trends, peaking at week 3 with a reciprocal serum endpoint titer of *ca.* 300 (Fig. 6*C*). We boosted the mice 7 wk after the initial injection and measured the resulting antibody response over the subsequent 8 wk (*SI Appendix*, Fig. S17). As expected, both treatments showed a continual increase in titer that tapered by the fourth week. Interestingly, Ova@NU-1003 produced weaker titers following the third injection at week 7, peaking at a reciprocal serum titer of *ca.* 600 at week 11, *ca.* ninefold lower than the Ova@NU-1000 titer (*ca.* 7000, Fig. 6*C*). While these antibody titers subsequently decreased through to week 15, as expected with no additional boosts, even at week 15, Ova@NU-1000-induced titers remained significantly elevated above those induced by Ova@NU-1003. In contrast, mice immunized with Ova@NU-1003 exhibited titers below those of the initial prime-boost. These results provide insights into how release-driven differences propagate varied T cell profiles and ultimately impact long-term humoral immunity. As long-term humoral responses are influenced by $CD4^+$ T cells, these results corroborate how Ova@NU-1000 induces a stronger long-term $CD4^+$ T cell memory compared to Ova@NU-1003, which biases toward a stronger $CD8^+$ T cell response. We hypothesize that while differences in the $CD4^+$ and $CD8^+$ T cell profiles did not impact initial humoral responses between Ova@NU-1000 and Ova@NU-1003, it produced significant differences in long-term antigen-specific humoral responses due to increased $CD4^+$ T cell–mediated enhancement with Ova@NU-1000.

This nuance in the $CD4^+$ T cell response was investigated through differences in the IgG isotypes produced. The ratio of T_H2:T_H1 polarization was investigated by comparing the amount of generated ovalbumin-specific IgG1 to IgG2a antibodies during the peak on week 11. Ova@NU-1000 immunization induced a *ca.* 1.74-fold higher ratio of IgG1:IgG2a compared to admix, while Ova@NU-1003 induced *ca.* 3.39-fold lower ratio compared to admix (Fig. 6*D*). This highlightes that Ova@NU-1000 induces a stronger antigen-specific humoral response and Ova@NU-1003 biases toward a T_H1 response, which can be implicated in protection from various infectious diseases (50, 51).

MOF-induced Differences in Raised Humoral Immunity Translate to SARS-CoV-2 RBD Antigen. We sought to translate the observed findings to a clinically relevant antigen and selected the SARS-CoV-2 spike receptor binding domain (RBD). Wild-type RBD was loaded at *ca.* 0.25 mg/mg of RBD to MOF (RBD@NU-100x), which

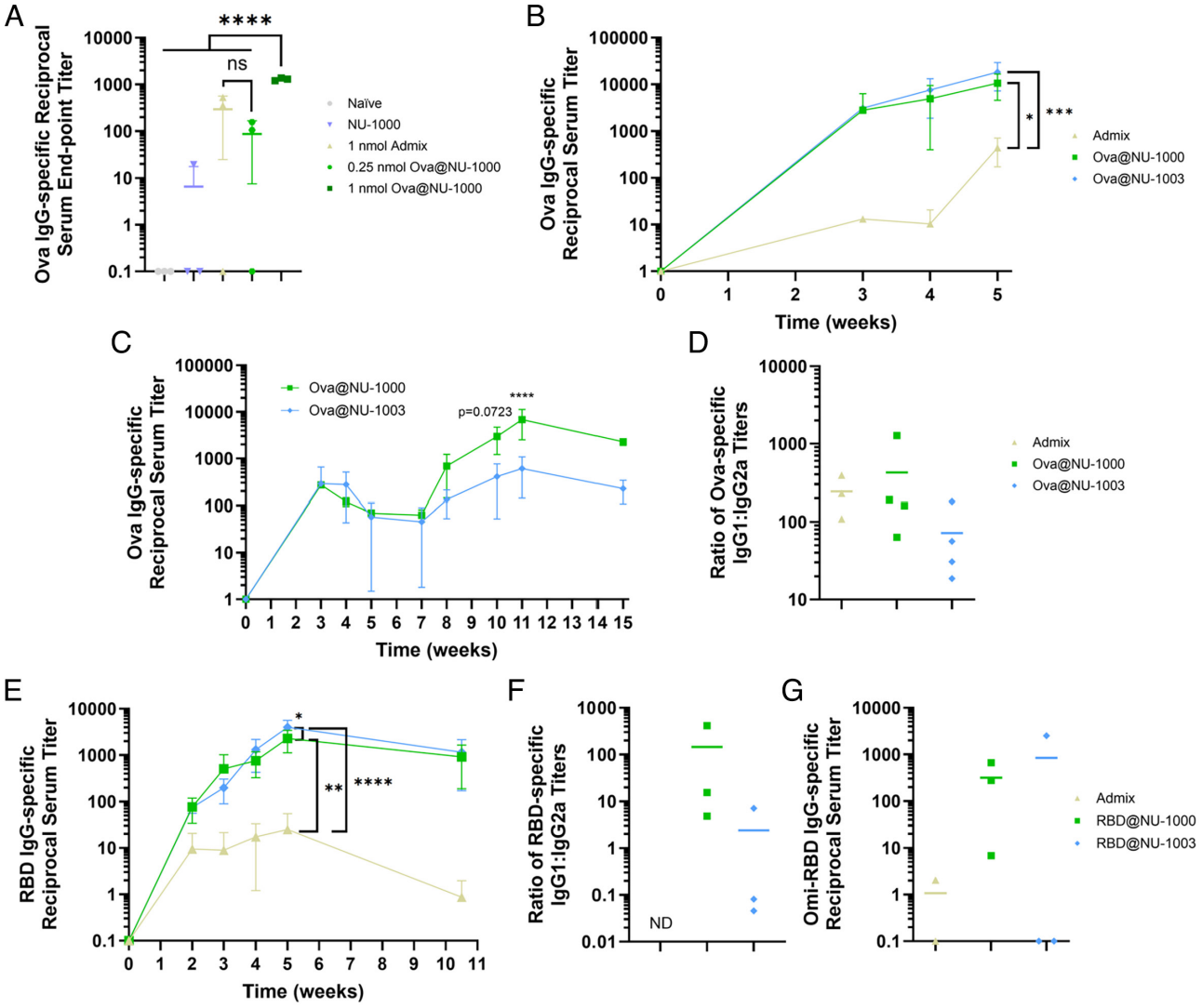

Fig. 6. Antigen-loaded NU-1000 and NU-1003 elicit strong and distinct antibody responses over time in vivo in female C57BL/6 mice with both Ova and RBD. (*A*) Ovalbumin-specific IgG reciprocal titers comparing the effects of dosage and MOF encapsulation on the humoral response on day 21, with immunizations at a 1:1 dose of Ova and ODN1826 as an admix or ODN1826 and Ova@NU-1000 on day 0 and 7 (n = 3 per group). (*B*) Ovalbumin-specific IgG reciprocal titers over time from ovalbumin and ODN1826 administered as an admix or coencapsulated in Adj-Ova@NU-100x (n = 3 per group). Mice were primed on day 0, then boosted on week 2 and week 4. Blood collections for serum occurred on weeks 3 to 5. (*C*) Long-term comparison of humoral responses between Ova@NU-1000 and Ova@NU-1003 with free ODN1826 (n = 2-3 per group), based on the injection schedule in *SI Appendix*, Fig. S17. (*D*) Difference in the ratio of ovalbumin-specific T_H2-induced IgG1 to T_H1-induced IgG2a reciprocal titers (n = 3-4 per group). (*E*) Wild-type RBD-specific IgG reciprocal serum titers from wild-type RBD and ODN1826 administered as an admix or RBD@NU-1000 and RBD@NU-1003 with free ODN1826 (n = 2-3 per group) based on injection and blood collection schedule in *SI Appendix*, Fig. S20. (*F*) Difference in the ratio of RBD-specific T_H2-induced IgG1 to T_H1-induced IgG2a reciprocal titers. (*G*) Omi-RBD-specific IgG reciprocal titer in mice following the aforementioned vaccination using wild-type RBD. Mean and SD shown in panels *A*–*C* and *E*. In panel *A*, analysis was performed using an ordinary one-way ANOVA followed by Tukey's multiple comparisons test. In panels *B*, *C*, and *E*, analysis was performed using an ordinary two-way ANOVA, followed by Šídák's (*B* and *D*) or Tukey's (*C*) multiple comparisons test. *$P < 0.05$; **$P < 0.01$; ***$P < 0.001$; ****$P < 0.0001$; ns = nonsignificant. Not all significances are shown for clarity.

encompassed nearly 100% encapsulation efficiency (*SI Appendix*, Figs. S18 and S19). To investigate humoral immunity, female C57BL/6 mice (n = 2-3) were injected with 1.5 nmol of wild-type RBD antigen as either RBD@NU-1000 or RBD@NU-1003 with 1.5 nmol of ODN1826 adjuvant on weeks 0 and 2. Blood draws were done on weeks 2 to 5 and 10.5 to measure RBD-specific IgG titers (*SI Appendix*, Fig. S20). While all groups showed an overall increase in RBD-specific IgG reciprocal serum titers, RBD@NU-1000 displayed *ca.* 137-fold higher titer compared to the admix, while RBD@NU-1003 displayed *ca.* 240-fold higher titer at 5 wk postprime (Fig. 6*E*). Both MOF treatments maintained strong long-term titers 2 mo following the boost (*ca.* 900 and 1100 for RBD@NU-1000 and RBD@NU-1003, respectively) (Fig. 6*E*). We measured the ratio of T_H2:T_H1 polarization based on the RBD-specific IgG isotypes. Consistent with the ovalbumin responses, RBD@NU-1000 induced the greatest ratio of RBD-specific IgG1:IgG2a titer at *ca.* 145.7, which was *ca.* 60.5-fold greater than RBD@NU-1003 (Fig. 6*F*). We also investigated how MOF-induced antigen release kinetics could promote humoral protection against mutant variants of the loaded antigen. With week 5 serum from mice immunized with wild-type RBD, we assessed the breadth of binding antibodies raised via production of antigen-specific IgG antibodies against the Omicron RBD variant (Omi-RBD). We observed that RBD@NU-1000 raised antibodies that more consistently bound to Omi-RBD compared to those raised from RBD@NU-1003 vaccination (Fig. 6*G*). This supports that RBD@NU-1000 raises a greater breadth of epitope recognition despite a comparable wild-type RBD-specific IgG titer to RBD@NU-1003. This key difference has major clinical implications in designing vaccines that can remain effective against constantly evolving and evasive viral variants.

Discussion

This work explores the importance of intracellular antigen release rate on raising adaptive immune responses and illustrates how it can be harnessed to bias immune populations. We uncovered that slower intracellular antigen release skews the T cell population toward a stronger $CD8^+$ over $CD4^+$ response. The slower kinetics also modulate T_H1 and T_H2 responses, elevating T_H1 polarization and the cellular adaptive immune response. These nuances in antigen release rate of native, unmodified protein are possible through use of MOF nanoparticles. By harnessing the NU-100x series MOFs, we altered antigen release rate solely through changing the pore size in these channel-type MOF structures. The MOF nanoparticles encapsulated high amounts (up to 1.4 mg/mg) of native, unmodified protein that is effectively processed by BMDCs in a specific manner to stimulate variable antigen-specific T cell responses driven by antigen release rate. Altering antigen release rate of native, unmodified protein using these nanomaterials circumvents traditional genetic engineering approaches that risk mutating key amino acid residues. Moreover, this approach does not require detailed analysis of the protein structure prior to implementation with this vaccine platform.

Antigen release rate as a tunable parameter can be further modified with these MOF nanoparticles facilely through alterations to the MOF linkers to vary the pore size and pore channel shape. We observed how changing antigen release resulted in profound effects on the raised T cell profiles. These effects were corroborated by in vivo studies, where mice immunized with Adj-Ova@NU-100x induced strong antibody responses over 5 wk. The larger pores of NU-1003 biased a strong ovalbumin-specific $CD8^+$ T cell response, and a weaker $CD4^+$ T cell response that skewed toward the T_H1 phenotype. This was in contrast with NU-1000, which induced both strong ovalbumin-specific $CD8^+$ and $CD4^+$ T cell responses, as well as a $CD4^+$ T cell–mediated humoral response. These findings were translated to the clinically relevant SARS-CoV-2 RBD antigen, where we showed that RBD@NU-1003 induced a similar skew in RBD-specific IgGs toward the T_H1 phenotype. Notably, we observed that NU-1000-mediated release of antigen more consistently generated antibodies with a greater breadth of epitope recognition compared to NU-1003, measured through their binding capabilities to the Omicron RBD variant, even when the vaccines solely delivered wild-type RBD. Thus, our data show distinct differences between NU-1000 and NU-1003 and their utility in elucidating not solely how MOF pore size can modulate antigen release kinetics, but the impact of modulated antigen release kinetics as a handle for T cell polarization, and antibody specificity and breadth in a vaccine platform. The key role that antigen release plays was uniquely unpacked herein without affecting protein antigen structure. As such, the principles uncovered can be applied to define antigen release rate profiles in other nanocarrier systems as a path toward personalized vaccine responses. Overall, our findings highlight the importance of integrating antigen release kinetics into vaccine design to maximize their efficacy, and the potential to affect, elongate, and broaden vaccine responses without affecting antigen composition in the vaccine. These findings can be harnessed to develop personalized vaccines tailored for various diseases using off-the-shelf native protein antigens.

Materials and Methods

Materials and Animals. Unless otherwise noted, all reagents were purchased commercially and used as received. C57BL/6, C57BL/6-Tg(TcraTcrb)1100Mjb/J (OT-I) and B6.Cg-Tg(TcraTcrb)425Cbn/J (OT-II) mice (female, ages 6–8 wks) were purchased from Jackson Laboratory. All national and local guidelines and regulations were followed when handling mice, and all protocols were approved by the institutional animal care and use committee at Boston University. Water was filtered through a Milli-Q water purification system. Zirconium(IV) chloride, zirconyl chloride octahydrate (≥98%), and trifluoroacetic acid (TFA) (≥99%) were purchased from Sigma-Aldrich. Zirconium(IV) chloride was stored in an Ar-filled nitrogen glove box. Glacial acetic acid, hydrochloric acid (37%), N,N-dimethylformamide (DMF) (99.9%), and acetone (99.8%) were purchased from Fisher Scientific. All DNA synthesis reagents were purchased from Glen Research.

Synthesis of NU-1000 (100 to 200 nm). Stock solution A was prepared with 400 mg zirconium chloride dissolved in 50 mL DMF. Stock solution B was prepared by dissolving 100 mg H4TBaPy linker in 50 mL DMF. Each solution was fully dissolved via sonication for 5 min. In a 2-dram vial, 2 mL A and 2 mL B were combined along with 0.8 mL glacial acetic acid and 0.4 mL deionized water. The solution was vortexed and placed immediately into a preheated oil bath. Agitation of the clear bright yellow solution was avoided once placed in an oil bath at 120 °C. The solution was removed from the oil bath and placed in an ice bath once it began to turn cloudy after 3 to 5 min, yielding particles between 100 to 200 nm. Once the reaction cooled, NU-1000 particles were isolated through centrifugation (8,000 rpm, 20 min) and washed with 5 mL DMF in a 15 mL centrifuge tube. Batches yielded relatively homogenous particles with minimal variability (about 4 mg of MOF per batch). Particle size was determined by SEM. Batches containing similar size particles were combined and washed with DMF solution 2×, with a 1 h soaking period in between (scale wash solvent amount by 4 mL per vial of reaction). After the last wash, particles were isolated and washed in an acidified DMF solution (1.2 mL DMF and 0.05 mL 8 M aq. HCl per batch) for 18 h in a 100 °C oven. Once cooled to room temperature (RT), MOF crystallites were washed with DMF 3× and then with acetone 3× with 1 h soaking in between. Nano NU-1000 was kept in acetone for long term storage. Immediately before use, the MOF was activated thermally in a vacuum oven at 80 °C overnight.

Synthesis of NU-1003 (100 to 200 nm). Stock solution A was made with 200 mg zirconyl chloride octahydrate dissolved in 50 mL DMF and 0.75 mL of TFA. Stock solution B was made with 30 mg of H4TNaPy (1,3,6,8)-tetra(6-carboxy naphthalen-2-yl(pyrene) dissolved in 50 mL DMF. 10 mL A and 10 mL B were combined in a 10–20 mL Biotage microwave vial with a stir bar, and the solution was immediately subjected to microwave heating at 160 °C for 15 min, resulting in a yellow cloudy solution. Each batch of reaction yielded about 10 mg of NU-1003. The solution was then centrifuged at 8,000 rpm for 20 min to isolate the MOF particles, which were washed with 20 mL DMF 3×, with 1 h waiting time in between. The MOF particles were then incubated with 0.5 mL 8 M HCl and 12 mL DMF at 100 °C for 18 h, then washed with 20 mL DMF 3× and 20 mL acetone 3×. NU-1003 was kept in acetone for storage, and was solvent exchanged to an aqueous solution before encapsulation.

Activation of the Samples for N_2 adsorption Measurement. Prior to N_2 adsorption measurements, nano NU-1003 was activated with supercritical CO_2 on a Tousimis supercritical point dryer (5 purges, each with 2 h in between, and bled at 50 mL/min overnight) from ethanol, and nano NU-1000 was dried in an 80 °C vacuum oven from acetone overnight. Each sample was then activated thermally at 120 °C under vacuum overnight on a Micromeritics Smart VacPrep instrument. Porosity of the activated samples was then measured by isothermal N_2 adsorption at 77 K on Micromeritics Tristar II 3020.

Instrumentation for MOF Characterization. Supercritical activation was performed in a Tousimis supercritical point dryer. Thermal activation was performed on a Micromeritics Smart VacPrep instrument. Porosity measurements were conducted on Micromeritics Tristar II 3020. PXRD was collected on a STOE-STADI-P powder diffractometer operating at 40 kV voltage and 40 mA current with Cu-Kα1 X-ray radiation ($\lambda = 0.154056$ nm) in transmission geometry. SEM images were taken on Hitachi SU8030 and analyzed using ImageJ.

Antigen Encapsulation into NU-100x. Ovalbumin (Abnova) or SARS-CoV-2 RBD (GenScript) was loaded into MOFs postsynthesis. For NU-1000, 0.25 mg was resuspended in 500 μL Milli-Q water and sonicated for 20 seconds. For NU-1003, 0.25 mg suspended in acetone was solvent exchanged by washing 3 times with Milli-Q water. Samples were subsequently soaked in 500 μL of 100 μM ovalbumin in Milli-Q water or 400 μL of 5 μM RBD in 1× Tris-buffered saline (TBS) and 2 mM ethylenediaminetetraacetic acid (EDTA) for 24 h in a 25 °C thermal mixer at 300 rpm. After loading, samples were centrifuged (14,800 rpm, 1 min) and the

supernatant was saved for quantification. Samples were washed twice in 500 μL of Milli-Q water, then stored at 4 °C until use. Supernatant protein concentration was quantified using a Pierce™ BCA Protein Assay Kit (Thermo Scientific) following the manufacturer's instructions and read using a SpectraMax i3X plate reader. Loading capacity was calculated as the mass of loaded ovalbumin over the mass of incubated MOF. To load fluorescent ovalbumin into MOFs, 0.2 mg of either NU-1000 or NU-1003 was incubated in 400 μL of 1.25 μM Alexa Fluor 555 (AF555)-conjugated ovalbumin (Ova-AF555; Invitrogen) or 20 μM Ova-AF647 (Invitrogen) for 24 h in a 25 °C thermal mixer at 300 rpm. After loading, samples were centrifuged, washed, and stored as described above. Supernatant protein concentration was quantified using ultraviolet (UV)-Vis absorption at 555 nm or 650 nm with an extinction coefficient of 155,000 $cm^{-1}M^{-1}$ or 239,000 $cm^{-1}M^{-1}$ for Ova-AF555 and Ova-AF647, respectively, on an Agilent Cary 60 spectrophotometer.

NU-100x Antigen Release. 0.2 mg of Ova-AF555@NU-1000 and Ova-AF555@NU-1003 were incubated in 500 μL acidic 1× PBS (pH 6.5) with 10% FBS in a 37 °C thermal mixer at 300 rpm for the appropriate timepoints, shown on the graph. At the specified timepoints, MOFs were centrifuged (14,800 rpm, 2 min) to pellet them out and supernatant was collected for analysis. After the final timepoint, MOFs were washed with Milli-Q water then incubated with 10× PBS for 24 h to release all cargo. All supernatants were stored at −80 °C for simultaneous analysis. Once all samples were collected, supernatants were loaded into a 10% native polyacrylamide gel, which was run at 200 V for 1 h. Gels were imaged using a gel imager (ChemiDoc). Samples were normalized to the total protein released using ImageJ to determine the cumulative release over time. Derivatives of release were calculated as the slope between adjacent timepoints.

NU-100x Uptake. Hindlegs from C57BL/6 mice were harvested for the collection of bone marrow–derived dendritic cells (BMDCs). Cells were flushed from the bone marrow using Roswell Park Memorial Institute 1640 Medium (RPMI, Gibco) containing 10% heat inactivated fetal bovine serum (Gibco), 1% penicillin/streptomycin (Gibco) (RPMI+/+) through a syringe. The cell suspension was centrifuged (1,200 rpm, 5 min) and supernatant aspirated. Red blood cells were lysed using 2 mL of ACK lysing buffer (Gibco) for 4 min at RT. Cells were washed with 1× PBS (Gibco) and cultured in 100 mm petri dishes in 20 mL of RPMI+/+ with 40 ng/mL granulocyte–macrophage colony-stimulating factor (GM-CSF, BioLegend) for 7 d in an Isotemp CO_2 incubator (Thermo Fisher). 10 mL of RPMI+/+ was added after day 4 to maintain appropriate nutrients. Cells were scraped, transferred to microtiter tubes (Thermo Scientific, 1.2×10^5 cells/tube), and let sit for 1 h prior to treatment. Cells were treated with 0.05 mg of Ova@NU-1000 or Ova@NU-1003 (by MOF mass) for 1, 3, 6, 10, or 24 h in a 37 °C/5% CO_2 incubator. At the specified timepoints, cells were washed with PBS and centrifuged (1200 rpm, 5 min) to remove supernatant and stained with fluorophore-conjugated antibodies: CD11c–Alexa Fluor 647 (BioLegend, #117312) and Fixable Live/Dead-Red (Invitrogen) for 25 min at 4 °C. Cells were washed with PBS, resuspended in 100 μL 4% paraformaldehyde (PFA) fixation buffer (BioLegend), and incubated at 4 °C until analysis using an Attune NxT flow cytometer. Uptake was analyzed using the inherent MOF fluorescence at 387 nm from a 488 nm excitation laser.

Synthesis and Purification of ODN1826. ODN1826 was synthesized using a MerMade 12 (LGC Biosearch Technologies) using standard phosphoramidite chemistry with phosphorothioate backbones, as previously reported (52). Strands were deprotected as previously reported using a 1:1 solution of 37% ammonium hydroxide/40% methylamine (Sigma) at 55 °C for 35 min (52). Reverse phase high-performance liquid chromatography (Agilent) was performed on a C18 column (Agilent), using a gradient of: 0.1 M triethylammonium acetate and 3% acetonitrile (ACN) in water; and 100% ACN. Fractioned samples were lyophilized and incubated with 20% aqueous acetic acid at RT for 1 h, followed by 3 washes with ethyl acetate (Sigma). Products were lyophilized and resuspended in MilliQ water, and quantified via UV-vis absorption at 260 nm (Extinction coefficients calculated through IDT OligoAnalyzer) (*SI Appendix*, Table S1). Molecular weights were confirmed using matrix-assisted laser desorption/ionization time-of-flight (Bruker).

In Vitro Ovalbumin-specific Antigen Presentation. BMDCs were harvested, cultured, and transferred to microtiter tubes as described above in the NU-100x Uptake section. BMDCs (2.5×10^5 cells/tube) were then treated with a 1:1 ratio of 2.5 μM of ODN1826 and 2.5 μM ovalbumin free in solution or encapsulated in Ova@NU-100x for 24, 48, or 72 h at 37 °C and 5% CO_2. Cells incubated for 48 or 72 h were given 100 μL of RPMI+/+ after every 24 h. At the specified timepoints, cells were washed with PBS and centrifuged (1,200 rpm, 5 min) to remove supernatant and incubated with blocking antibodies (BioLegend #156604) for 10 min at 4 °C. Cells were then stained with fluorophore-conjugated antibodies: CD11c–PE (BioLegend, #117308); SIINFEKL–PE-Cy7 (BioLegend, #141608); CD80–PerCP-Cy5.5 (BioLegend, #104722); Fixable Live/Dead-Far Red (Invitrogen) for 25 min at 4 °C. Cells were washed with PBS and centrifuged (1,200 rpm, 5 min) to remove supernatant, resuspended in 100 μL 4% PFA, and incubated at 4 °C until flow cytometry.

Endolysosomal Compartment Microscopy Analysis. 12 mm #1.5 glass coverslips (Carolina) were sterilized with 70% ethanol followed by UV light for 20 min. Wells were washed 4× with PBS and coated with 50 μg/mL poly-D-lysine (PDL; Gibco) for 1 h at RT. Wells were washed 4× with sterile deionized water and kept at 4 °C until use. BMDCs were harvested as described above, then further isolated using the EasySep™ Mouse Biotin Positive Selection Kit II (STEMCELL Technologies). Cells were then washed with RPMI+/+, resuspended at 3×10^5 cells/mL, and added to the PDL-coated coverslips (1.5×10^5 cells/well) overnight at 37 °C and 5% CO_2. Supernatant was removed and cells were treated with 100 nM of AF647-conjugated Ova as Ova-AF647@NU-100x for 4 or 24 h. Cells were washed with PBS, then fixed with 2% PFA for 15 min at RT. Cells were washed 4× with PBS, then permeabilized using PBS containing 0.5% Tween-20 (Thermo Scientific) for 5 min at RT. Afterward, cells were washed 4× with PBS, then blocked using PBS containing 10% FBS for 1 h at RT. Cells were then incubated with organelle-specific primary antibodies [EEA1 (1:1,000; Abcam) or LAMP1 (1:400; Abclonal)] for 24 h at 4 °C. Samples were washed 4× with PBS and stained with AF555-conjugated secondary antibodies (1:1,000; Abclonal) for 45 min at RT. Cells were washed 4× with PBS, mounted onto a glass slide using ProLong Gold Antifade Mountant (Invitrogen), and sealed with clear nail polish for 24 h. Samples were imaged with the Nikon CSU-W1 SoRA Spinning Disk Confocal Microscope using a 60× 1.27 NA water immersion objective and 2.8× SoRA magnifier using the Nikon NIS-Elements AR software. Images were denoised using the built-in Denoise.ai tool, then analyzed in ImageJ to determine the Mander's overlap coefficient using the JACoP plugin (53).

In Vitro Splenocyte Proliferation. Spleens were harvested from OT-I or OT-II mice and strained through a 70 μm strainer using a continuous flow of PBS. Cells were centrifuged (1,200 rpm, 5 min) and the supernatant aspirated and replaced with 3 mL of ACK lysing buffer for 7 min at RT to selectively lyse red blood cells. Remaining cells were washed and resuspended in PBS at 4×10^7 cells/mL. Cells were stained with eFluor670 (Invitrogen) following manufacturer instructions. Cells were resuspended in RPMI+/+ and plated in a 96-well round bottom plate (3×10^5 cells/well) with varying concentrations of ovalbumin either free in solution or in Ova@NU-100x for 3 to 4 d. At the specified timepoints, cells were centrifuged (1,200 rpm, 5 min), and the supernatant was collected for cytokine analysis. Cells were washed with PBS and centrifuged (1,200 rpm, 5 min) to remove supernatant and stained with either CD4–PE (BioLegend, #100408) or CD8a–PE (BD, #553033) for 25 min at 4 °C. Cells were washed with PBS and analyzed via live flow cytometry. Dose–response data were fit using a four-parameter Hill equation.

In Vitro Pooled Splenocyte Proliferation. As described above, spleens were harvested and stained with eFluor670 for OT-II cells and eFluor450 (Invitrogen) for OT-I cells. A 1:1 ratio of OT-I and OT-II cells were plated in a 96-well plate (3×10^5 cells/well) and incubated with varying concentrations of ovalbumin either free in solution or in Ova@NU-100x for 3 to 5 d at 37 °C and 5% CO_2. At the specified timepoints, cells were centrifuged (1,200 rpm, 5 min), and the supernatant was collected for cytokine analysis. Cells were subsequently washed with PBS and centrifuged (1,200 rpm, 5 min) to remove supernatant and stained with CD4–PerCP-Cy5.5 (BioLegend, #100434) and CD8a–PE for 25 min at 4 °C. Cells were washed with PBS and analyzed via live flow cytometry. Dose–response data were fit using a four-parameter Hill equation.

In Vitro Cytokine Production. Supernatant collected from OT-II or pooled OT-I and OT-II splenocytes 4 d following incubation were analyzed for IFN-γ and IL-5 cytokines using an ELISA following manufacturer instructions (BioLegend). Plates were immediately read at 450 nm, and sample concentrations were determined by fitting a sigmoidal logistic regression standard curve. The 570 nm background was also read and subtracted from the 450 nm reading as needed.

Ovalbumin and ODN1826 Coencapsulation into NU-100x. ODN1826 was loaded first into MOFs by incubating 0.20 mg of either NU-1000 or NU-1003 in 400 μL of 10 μM ODN1826 dissolved in water for 4 h at 37 °C at 300 rpm. Samples were centrifuged (14,800 rpm, 2 min), and the supernatant was saved for quantification. Samples were washed twice in 500 μL Milli-Q water, then stored at 4 °C. Supernatant adjuvant concentration was quantified using UV-Vis absorption at 260 nm with an extinction coefficient of 181,100 cm^{-1} M^{-1}. Ovalbumin was subsequently loaded into MOFs by incubating samples in 500 μL of 30 μM ovalbumin. Samples were washed, stored, and quantified as described in the Ovalbumin Encapsulation into NU-100x section. Adj-Ova@MOF samples were pooled to generate a 1:1 loading ratio of ovalbumin to ODN1826 for all experiments.

In Vivo Treatment for Lymphocyte Isolation, ELISpot Assay, and Ovalbumin-Specific Antibodies. Female C57BL/6 mice (n = 3 to 4 per group) were subcutaneously administered three injections of 2 nmols ovalbumin and 2 nmols ODN1826 every two weeks, either as an admix or coencapsulated in Adj-Ova@NU-100x. Spleens from all mice were harvested 5 wk after the initial injection, filtered through 70 μm strainers, washed, and counted as previously described, then resuspended at a concentration of 1×10^8 cells/mL in RPMI+/+ for subsequent experiments. Murine blood was also collected 3, 4 (retroorbital), and 5 (cardiac puncture) weeks after the initial injection, as described below.

T Cell Memory Phenotyping. Splenocytes were transferred to microtiter tubes (3×10^6 cells/tube), washed with PBS, and stained with fluorophore-conjugated antibodies: CD4–PE; CD8a–APC (BD, #553035); CD44–V450 (BD, #560451); CD62L–PE-Cy7 (BD, #560516); Fixable Live/Dead-Green (Invitrogen) for 25 min at 4 °C. Cells were washed with PBS and centrifuged (1,200 rpm, 5 min) to remove supernatant, resuspended in 100 μL 4% PFA, and incubated at 4 °C until analysis by flow cytometry. Effector memory T cells were identified as $CD44^+CD62L^-$.

T Cell Ovalbumin Specificity. The day before harvesting splenocytes, DimerX I:PE H-2 Kb:Ig fusion protein (BD, #550750) was incubated with Ova1 according to the manufacturer's protocol. Splenocytes were transferred to microtiter tubes (1×10^6 cells/tube), washed with PBS, and stained with fluorophore-conjugated antibodies. For Ova1-specific $CD8^+$ T cells: CD4–PerCP-Cy5.5; CD8a–FITC (BD, #553031); Ova1-DimerX I:PE; Fixable Live/Dead-Violet (Invitrogen) for 25 min at 4 °C. For Ova2-specific $CD4^+$ T cells: cells were stained with Ova2 Tetramer–APC (ProImmune) for 2 h at 37 °C, washed with PBS, then stained with CD4–PerCP-Cy5.5; CD19–PE (BD, #152408); Fixable Live/Dead-Green for 25 min at 4 °C. Cells were washed with PBS and resuspended in 100 μL 4% PFA, and incubated at 4 °C until flow cytometry.

ELISpot Assay. An IFN-γ ELISpot was performed following the manufacturer's instructions (BD). To 2×10^5 splenocytes in 100 μL RPMI+/+, 100 μL of either (final concentration): Ova1 (5 μg/mL), nonspecific peptide (KRAS, 5 μg/mL), anti-CD3ε (BioLegend, #100340), and anti-CD28 (BioLegend, #102116) (2 μg/mL each, positive control), or RPMI+/+ media (negative control) solutions were added. Plates were incubated in 37 °C and 5% CO_2 for 48 h. The plate was washed, and detection antibody, enzyme conjugate, and chromogenic substrate (BD) were added. Once sufficient spots formed, wells were washed with deionized water and air-dried at RT overnight. Samples were stored in the dark until analyzed using a CTL ImmunoSpot imager.

Antigen-Specific IgG, IgG1, and IgG2a Binding Antibodies via ELISA. Uncoated ELISA plates were coated with 100 μL of 2.5 μg/mL ovalbumin, RBD, or Omi-RBD in 1× coating buffer at 37 °C for 2 h. After coating, wells were washed and blocked with PBS containing 10% FBS and 0.1% Tween-20 at 37 °C for 2 h. Mouse sera were diluted in 1× ELISA dilution buffer. Blocking solution was removed and 100 μL of diluted sample was added to each well and incubated for 1 h at 37 °C. Wells were washed 4× with PBS containing 0.1% Tween-20, then incubated with 100 μL of either goat anti-mouse IgG-HRP (1:4000, BioLegend, #405306), goat anti-mouse IgG1-HRP (1:1,000, Invitrogen, #A10551), or goat anti-mouse IgG2a-HRP (1:1,000, Invitrogen #A-10685) in 1× ELISA dilution buffer for 1 h. Wells were washed 4×, then incubated with 100 μL of a 1:1 mixture of TMB Reagent A and Reagent B. Plate was incubated in the dark for 5 to 20 min, after which 100 μL of TMB Stop Solution was added. Plates were immediately read at 450 nm and 570 nm. Titers were defined as the reciprocal serum dilution where the difference between 450 nm and 570 nm absorbances was at least 0.3 (RBD IgG isotypes only) or 0.5 units above the background (i.e., naïve sera). The ratio was determined by dividing the two titers.

Retroorbital Blood Collection. Mice were anesthetized using vaporized isoflurane (Sigma-Aldrich). Once under, a glass Pasteur pipette coated with *ca.* 30 to 50 μL heparin (Sigma-Aldrich, 55.6 mg/mL) was inserted through the conjunctiva and into the orbital sinus by quickly rotating the pipette to collect ~100 μL of blood. Drawn blood was stored at RT for >30 min to clot, then centrifuged at 1,000 × g for 10 min. The serum supernatant was transferred to a 96-well plate and stored at −80 °C until analysis.

Cardiac Puncture Blood Collection. A syringe coated with *ca.* 30–50 μL heparin (55.6 mg/mL) was used to puncture the mouse just below the ribcage to draw blood from the heart. Samples were clotted, centrifuged, and stored as described above in the Retroorbital Blood Collection section.

Effect of Dosage and Free MOF on Ovalbumin-specific Antibody Response. Female C57BL/6 mice (n = 3 per group) were subcutaneously administered two injections of one the following conditions: 1 nmol of ovalbumin and 1 nmol ODN1826 (admix or mix of Ova@NU-1000 and free ODN1826); 0.25 nmol of ovalbumin and 0.25 nmol ODN1826 (mix of Ova@NU-1000 and free ODN1826); free NU-1000 (MOF mass matched to highest Ova@NU-1000 + ODN1826 condition), spaced 1 wk apart. Three weeks after the initial injection, murine blood was collected via cardiac puncture to analyze ovalbumin-specific antibody responses using the methods described above.

Long-Term Ovalbumin-Specific Antibody Response. Female C57BL/6 mice (n = 2 to 4 per group) were subcutaneously administered two injections of 1 nmol of ovalbumin and 1 nmol ODN1826 as a mix of Ova@NU-1000 and free ODN1826, spaced 1 wk apart. Retroorbital blood collection was performed on weeks 3, 4, 5, and 7 after the initial injection. Mice were boosted 7 wk after the initial injection. Blood was collected 1, 3, 4, and 8 wk after this boost.

RBD-Specific Antibody Response. Female C57BL/6 mice (n = 2 to 3 per group) were subcutaneously administered two injections of 1.5 nmol of RBD and 1.5 nmol ODN1826 as an admix or a mix of RBD@NU-100x and free ODN1826, spaced 2 wk apart. Retroorbital blood collection was performed 2 to 5 and 10.5 wk after the initial injection to analyze RBD-specific antibody responses using the methods described above. Blood collected on week 4 was also used to analyze RBD-specific IgG subtypes, while blood collected on week 5 was also used to analyze Omi-RBD-specific antibody responses.

Statistical Analysis. All results are shown as the mean ± SD or SEM, as described. Each point represents individual biological replicates; sample size shown in the caption. Statistical analysis was performed using GraphPad Prism 10 software, with the statistical analysis provided in the caption. An unpaired two-tailed *t* test was used to compare two groups, while an ANOVA with a post hoc test for multiple comparisons analysis was used to compare multiple groups. Proliferation curves were generated using a nonlinear, 4-parameter curve fit using a "Top" value based on the most proliferative condition to ensure EC_{50} could be generated. All microscopy images were first denoised using the Nikon Denoise.ai tool prior to analysis. Significance was defined as $P < 0.05$ ($^*P < 0.05$; $^{**}P < 0.01$; $^{***}P < 0.001$; $^{****}P < 0.0001$; ns = nonsignificant).

Data, Materials, and Software Availability. All study data are included in the article and/or *SI Appendix*.

ACKNOWLEDGMENTS. We would like to thank Dr. John Misasi, Ms. Antonina Puzyrova, Dr. Daniela Silva Ayala, and Dr. Nancy Sullivan for assistance with use of the ELISpot equipment, Dr. Xin Brown and Dr. Zahid Yaqoob for training on core equipment, and Dr. Yijing Chen for the initial development of nano NU-1000 synthesis. Research reported in this publication was supported by the Boston University Biointerface Technologies and Micro/Nano Imaging Core Facilities. M.H.T. acknowledges financial support from Boston University through startup funding support, as well as from the Arnold and Mabel Beckman Foundation through a Beckman Young Investigator Award. This work was supported in part by the National Institute of General Medical Sciences of the NIH award R35GM157326. E.C. acknowledges financial support from an NSF GRFP. E.C. and A.F. acknowledge support from the Translational Research in Biomaterials T32 training grant (T32EB006359). M.A.D. acknowledges support from the American Cancer Society (ACS IRG 22-153-42). J.A.N. acknowledges support from the Biological Design Center and STEM

Pathways of Boston University (DoD STEM FY20 Award HQ00342110008). M.I. acknowledges financial support from The Hartwell Foundation. F.S. and J.S.M acknowledge support from CBC U.S. Army Contracting Command (W52P1J-21-9-3023). F.S. also acknowledges support from the Ryan Fellowship and International Institute for Nanotechnology (IIN) at Northwestern University. PXRD measurements were performed at the IMSERC facility, which has received support from the Soft and Hybrid Nanotechnology Experimental (SHyNE) Resource (NSF ECCS-2025633), IIN, and Northwestern University. SEM measurements used the EPIC facility of Northwestern University's NUANCE Center, which has received support from the Soft and Hybrid Nanotechnology Experimental (SHyNE) Resource (NSF ECCS-2025633); the MRSEC program (NSF DMR-1121262) at the Materials Research Center; the IIN; and the State of Illinois, through the IIN.

Author affiliations: [a]Department of Biomedical Engineering, Boston University, Boston, MA 02215; [b]Department of Chemistry, Northwestern University, Evanston, IL 60208; and [c]Department of Materials Science and Engineering, Boston University, Boston, MA 02215

1. A. J. Pollard, E. M. Bijker, A guide to vaccinology: From basic principles to new developments. *Nat. Rev. Immunol.* **21**, 83–100 (2021).
2. J.-L.L. Excler, M. Saville, S. Berkley, J. H. Kim, Vaccine development for emerging infectious diseases. *Nat. Med.* **27**, 591–600 (2021).
3. H. D. Marston, G. K. Folkers, D. M. Morens, A. S. Fauci, Emerging viral diseases: Confronting threats with new technologies. *Sci. Transl. Med.* **6**, 253ps10 (2014).
4. P. M. Moyle, I. Toth, Modern subunit vaccines: Development, components, and research opportunities. *ChemMedChem* **8**, 360–376 (2013).
5. I. Mellman, S. J. Turley, R. M. Steinman, Antigen processing for amateurs and professionals. *Trends Cell Biol.* **8**, 231–237 (1998).
6. S. Scheiblhofer, J. Laimer, Y. Machado, R. Weiss, J. Thalhamer, Influence of protein fold stability on immunogenicity and its implications for vaccine design. *Expert Rev. Vaccines* **16**, 479–489 (2017).
7. A. C. Anselmo, Y. Gokarn, S. Mitragotri, Non-invasive delivery strategies for biologics. *Nat. Rev. Drug Discov.* **18**, 19–40 (2019).
8. R. Pati, M. Shevtsov, A. Sonawane, Nanoparticle vaccines against infectious diseases. *Front. Immunol.* **9**, 2224 (2018).
9. D. J. Irvine, M. A. Swartz, G. L. Szeto, Engineering synthetic vaccines using cues from natural immunity. *Nat. Mater.* **12**, 978–990 (2013).
10. M. A. Davis, E. Cho, M. H. Teplensky, Harnessing biomaterial architecture to drive anticancer innate immunity. *J. Mater. Chem. B* **11**, 10982–11005 (2023).
11. J. A. Zuris *et al.*, Cationic lipid-mediated delivery of proteins enables efficient protein-based genome editing in vitro and in vivo. *Nat. Biotechnol.* **33**, 73–80 (2015).
12. R. M. Haley *et al.*, Lipid nanoparticle delivery of small proteins for potent in vivo RAS inhibition. *ACS Appl. Mater. Interfaces* **15**, 21877 (2023).
13. Y. B. Kim, K. T. Zhao, D. B. Thompson, D. R. Liu, An anionic human protein mediates cationic liposome delivery of genome editing proteins into mammalian cells. *Nat. Commun.* **10**, 2905 (2019).
14. A. A. Eltoukhy *et al.*, Nucleic acid-mediated intracellular protein delivery by lipid-like nanoparticles. *Biomaterials* **35**, 6454–6461 (2014).
15. S. W. Howland, K. D. Wittrup, Antigen release kinetics in the phagosome are critical to cross-presentation efficiency. *J. Immunol.* **1950**, 1576–1583 (2008).
16. K. Skakuj, M. H. Teplensky, S. Wang, J. W. Dittmar, C. A. Mirkin, Chemically tuning the antigen release kinetics from spherical nucleic acids maximizes immune stimulation. *ACS Cent. Sci.* **7**, 1838–1846 (2021).
17. N. Chen *et al.*, Tunable degradation of acetalated dextran microparticles enables controlled vaccine adjuvant and antigen delivery to modulate adaptive immune responses. *J. Control. Release* **273**, 147 (2018).
18. K. E. Broaders, J. A. Cohen, T. T. Beaudette, E. M. Bachelder, J. M. J. Fréchet, Acetalated dextran is a chemically and biologically tunable material for particulate immunotherapy. *Proc. Natl. Acad. Sci. U.S.A.* **106**, 5497–5502 (2009).
19. S. Scheiblhofer, J. Laimer, Y. Machado, R. Weiss, J. Thalhamer, Influence of protein fold stability on immunogenicity and its implications for vaccine design. *Expert Rev. Vaccines* **16**, 479–489 (2017).
20. L. Delamarre, R. Couture, I. Mellman, E. S. Trombetta, Enhancing immunogenicity by limiting susceptibility to lysosomal proteolysis. *J. Exp. Med.* **203**, 2049–2055 (2006).
21. T. So, H.-O. Ito, M. Hirata, T. Ueda, T. Imoto, Contribution of conformational stability of hen lysozyme to induction of type 2 T-helper immune responses. *Immunology* **104**, 259–268 (2001).
22. O. K. Farha, J. T. Hupp, Rational design, synthesis, purification, and activation of metal—organic framework materials. *Acc. Chem. Res.* **43**, 1166–1175 (2010).
23. K. Lu, T. Aung, N. Guo, R. Weichselbaum, W. Lin, Nanoscale metal-organic frameworks for therapeutic, imaging, and sensing applications. *Adv. Mater.* **30**, e1707634 (2018).
24. P. Li *et al.*, Hierarchically engineered mesoporous metal-organic frameworks toward cell-free immobilized enzyme systems. *Chem* **4**, 1022–1034 (2018).
25. P. Li *et al.*, Toward design rules for enzyme immobilization in hierarchical mesoporous metal-organic frameworks. *Chem* **1**, 154–169 (2016).
26. O. K. Farha *et al.*, Metal-organic framework materials with ultrahigh surface areas: Is the sky the limit?. *J. Am. Chem. Soc.* **134**, 15016–15021 (2012).
27. M. H. Teplensky *et al.*, A highly porous metal-organic framework system to deliver payloads for gene knockdown. *Chem* **5**, 2926–2941 (2019).
28. M. H. Teplensky *et al.*, Temperature treatment of highly porous zirconium-containing metal-organic frameworks extends drug delivery release. *J. Am. Chem. Soc.* **139**, 7522–7532 (2017).
29. O. K. Farha *et al.*, De novo synthesis of a metal–organic framework material featuring ultrahigh surface area and gas storage capacities. *Nat. Chem.* **2**, 944–948 (2010).
30. S.-Y. Moon, Y. Liu, J. T. Hupp, O. K. Farha, Instantaneous hydrolysis of nerve-agent simulants with a six-connected zirconium-based metal-organic framework. *Angew. Chem.* **127**, 6899–6903 (2015).
31. M. P. Suh, H. J. Park, T. K. Prasad, D.-W. Lim, Hydrogen storage in metal-organic frameworks. *Chem. Rev.* **112**, 782–835 (2012).
32. J.-R. Li, J. Sculley, H.-C. Zhou, Metal-organic frameworks for separations. *Chem. Rev.* **112**, 869–932 (2012).
33. Z. H. Syed *et al.*, Metal-organic framework nodes as a supporting platform for tailoring the activity of metal catalysts. *ACS Catal.* **10**, 11556–11566 (2020).
34. A. Bavykina *et al.*, Metal-organic frameworks in heterogeneous catalysis: Recent progress, new trends, and future perspectives. *Chem. Rev.* **120**, 8468–8535 (2020).
35. S. Wang *et al.*, DNA-functionalized metal-organic framework nanoparticles for intracellular delivery of proteins. *J. Am. Chem. Soc.* **141**, 2215–2219 (2019).
36. S. K. Alsaiari *et al.*, Endosomal escape and delivery of CRISPR/Cas9 genome editing machinery enabled by nanoscale zeolitic imidazolate framework. *J. Am. Chem. Soc.* **140**, 143–146 (2018).
37. K. Ni *et al.*, Nanoscale metal-organic framework co-delivers TLR-7 agonists and anti-CD47 antibodies to modulate macrophages and orchestrate cancer immunotherapy. *J. Am. Chem. Soc.* **142**, 12579–12584 (2020).
38. T. Luo *et al.*, A 2D nanoradiosensitizer enhances radiotherapy and delivers STING agonists to potentiate cancer immunotherapy. *Adv. Mater.* **34**, 2110588 (2022).
39. K. Ni, T. Luo, G. T. Nash, W. Lin, Nanoscale metal-organic frameworks for cancer immunotherapy. *Acc. Chem. Res.* **53**, 1739–1748 (2020).
40. R. N. Ehrman *et al.*, A scalable synthesis of adjuvanting antigen depots based on metal–organic frameworks. *Chem. Sci.* **15**, 2731–2744 (2024).
41. M. Yu, J. Wu, J. Shi, O. C. Farokhzad, Nanotechnology for protein delivery: Overview and perspectives. *J. Control. Release Off. J. Control. Release Soc.* **240**, 24 (2015).
42. Z. Xu *et al.*, Protein–nanoparticle co-assembly supraparticles for drug delivery: Ultrahigh drug loading and colloidal stability, and instant and complete lysosomal drug release. *Int. J. Pharm.* **658**, 124231 (2024).
43. S. Behzadi *et al.*, Cellular uptake of nanoparticles: Journey inside the cell. *Chem. Soc. Rev.* **46**, 4218 (2017).
44. F. Sha *et al.*, Stabilization of an enzyme cytochrome c in a metal–organic framework against denaturing organic solvents. *iScience* **24**, 102641 (2021).
45. C. V. Harding, H. J. Geuze, Immunogenic peptides bind to class II MHC molecules in an early lysosomal compartment. *J. Immunol.* **151**, 3988–3998 (1993).
46. O. P. Joffre, E. Segura, A. Savina, S. Amigorena, Cross-presentation by dendritic cells. *Nat. Rev. Immunol.* **12**, 557–569 (2012).
47. G. Tau, P. Rothman, Biologic functions of the IFN-γ receptors. *Allergy* **54**, 1233–1251 (1999).
48. B. Spellberg, J. E. Edwards Jr., Type 1/type 2 immunity in infectious diseases. *Clin. Infect. Dis.* **32**, 76–102 (2001).
49. F. Y. Liew, TH1 and TH2 cells: A historical perspective. *Nat. Rev. Immunol.* **2**, 55–60 (2002).
50. J. P. Coutelier, J. T. van der Logt, F. W. Heessen, A. Vink, J. van Snick, Virally induced modulation of murine IgG antibody subclasses. *J. Exp. Med.* **168**, 2373–2378 (1988).
51. V. C. Huber *et al.*, Distinct contributions of vaccine-induced immunoglobulin G1 (IgG1) and IgG2a antibodies to protective immunity against influenza. *Clin. Vaccine Immunol.* **13**, 981–990 (2006).
52. M. H. Teplensky *et al.*, Spherical nucleic acid vaccine structure markedly influences adaptive immune responses of clinically-utilized prostate cancer targets *Adv. Healthc. Mater.* **10**, e2101262 (2021).
53. S. Bolte, F. P. Cordelières, A guided tour into subcellular colocalization analysis in light microscopy. *J. Microsc.* **224**, 213–232 (2006).